Supporting Information

Sharma et al. 10.1073/pnas.1220379110

SI Methods

To rationalize the structural and functional differences between the $\mathbf{O_H}$ and **O** states, we considered the property of inorganic Cu complexes of preferring a planar three-coordinate geometry when reduced, but four-coordinate geometries when oxidized (see *Rationale* in the main text). On this basis we constructed two models of the binuclear center (BNC), one in which Cu_B is only ligated by the three proteinaceous histidine ligands (trigonal) and another one in which there is an additional oxygenous ligand (a water or a hydroxyl) that might correspond to the activated ($\mathbf{O_H}$ and $\mathbf{F_H}$) and inactivated (**O** and **F**) states, respectively. The formal structures of the states that were optimized by density functional theory (DFT) calculations were as follows: **F** (Fe_{a3}[IV] = O^{2-}, Cu_B[II]–OH_2 and $TyrO^-$), **O** (Fe_{a3}[III]–OH^-, Cu_B[II] –OH_2 and $TyrO^-$), $\mathbf{F_H}$ (Fe_{a3}[IV] = O^{2-}, Cu_B[II] and $TyrO^-$), and $\mathbf{O_H}$ (Fe_{a3}[III]–OH^-, Cu_B[II] and $TyrO^-$) (Table S1 and Fig. S1). $\mathbf{F_H}$ and $\mathbf{O_H}$ are hypothetical "activated" variants of currently considered **F** and **O** structures and differ from these only by the lack of a fourth aquo ligand of Cu_B[II]. The model systems were constructed using the crystal structures of *Paracoccus denitrificans* and *Bos taurus* cytochrome *c* oxidase (C*c*O) (1, 2). The following functional groups of the active site were included in the models: iron porphyrin corresponding to heme a_3, its proximal histidine ligand, and Cu_B with its three histidine ligands, including the cross-linked tyrosine (Fig. S1). In all calculations tyrosine was kept deprotonated in agreement with the infrared data (see *Rationale* in the main text). The side-chains of the amino acid residues were cut at the Cβ positions, which were kept fixed during the DFT-based geometry optimizations. To avoid any large displacement of the porphyrin ring in the absence of surrounding protein, one or two *meso*-carbon atoms of the porphyrin ring were also kept fixed in some of the geometry optimizations. Two water molecules were included in the model systems. In "inactivated" states (**O** and **F**), one of the water molecule ligates the Cu_B ion and another one hydrogen bonds to the oxygenous ligand of heme a_3 and the cross-linked tyrosine, whereas in activated states ($\mathbf{O_H}$ and $\mathbf{F_H}$) both water molecules form a water network from the oxygenous ligand of heme a_3 to the cross-linked tyrosine, and Cu_B is only three-coordinated (Fig. S1). This scenario preserves the number of atoms and hydrogen bonds in the two systems ($\mathbf{O_H}$ and **O** and $\mathbf{F_H}$ and **F**). Similar DFT calculations were also made on other intermediate states, as described below.

Geometry optimizations were performed in different spin states (Table S1) at the BP86 level of theory (3, 4), applying the def2–SVP (split valence plus polarization) basis set on all C, H, N, and O atoms (5), and the def2–TZVP (triple zeta valence plus polarization) basis set on Fe and Cu atoms (6). Single-point calculations were then performed on the optimized geometries using the B3LYP hybrid density functional (7–9). At this stage, all atoms of the system were treated with the def2–TZVP basis set (6). Final energies were obtained at the dielectric constant ε = 4 (Table 1). TURBOMOLE (10) software was used for all of the DFT calculations, and the Conductor-like Screening Model (COSMO) (11) method implemented in TURBOMOLE was used for the continuum solvation treatment. All geometrical analyses of the optimized structures were performed with the Visual Molecular Dynamics (VMD) software (12) (Table S2).

To evaluate redox potentials (Table 2), the intermediate states $\mathbf{O_R}$, $\mathbf{O_{H,R}}$, $\mathbf{F_R}$, and $\mathbf{F_{H,R}}$ were optimized by DFT calculations. In these states an additional electron was transferred to the corresponding state of the BNC. The standard redox potentials (E^o) of the resulting redox couples $\mathbf{O_H}/\mathbf{O_{H,R}}$, $\mathbf{O}/\mathbf{O_R}$, $\mathbf{F_H}/\mathbf{F_{H,R}}$, and $\mathbf{F}/\mathbf{F_R}$ were evaluated from the calculated energies (B3LYP/def2–TZVP/ε= 4), using the formula:

$$E^o = \text{energy}_{\text{oxidized}} - \text{energy}_{\text{reduced}} - 4.43 \text{ Volts},$$

where the last term is the potential of the standard hydrogen electrode (13). The orbital populations (14) and spin densities obtained at the B3LYP/def2–TZVP/ε = 4 level of theory were also analyzed in different redox/spin states (Table S3). The spin densities were plotted using the VMD program (Fig. S2).

The magnetic coupling between the two metal centers of the BNC (Fe and Cu_B) can be ferromagnetic or antiferromagnetic in nature. To confirm that the energy differences between the two types of coupling are minimal, we performed additional Broken Symmetry (BS) calculations (15) on the model systems. The energies of low-spin antiferromagnetically coupled $S = 0$ (open-shell singlet), $S = 1$, and $S = 2$ spin states were obtained by performing single-point calculations on the high-spin ($S = 3$) geometry of **O**, $\mathbf{O_H}$, $\mathbf{F_R}$, and $\mathbf{F_{H,R}}$ states, by using the "spin-flip" feature available in TURBOMOLE, and followed by the Yamaguchi formulation (16, 17). Such procedures have been successfully applied in the past to obtain BS solutions and their energetics (18). Similarly, for **F** and $\mathbf{F_H}$ states BS solutions were generated from high-spin states, and energies were calculated, whereas no such attempt was made for the $\mathbf{O_R}$ and $\mathbf{O_{H,R}}$ states because in these states Cu_B was found to be reduced in accordance with the experimental data (see *The Metastable O_H State* in the main text and Table S3). The energies and spin densities from BS solutions are given in Table S4 and Table S3, respectively. It is to be stressed that the primary aim of these calculations was to show that the energy difference between the two types of coupling is minimal for all of the redox states studied here, and neither the energies nor the spin densities from BS solutions were used in any analysis because BS solutions were based on the geometries of high-spin cases.

It is known from experiments that the lifetime of the $\mathbf{O_H}$ state is in the range of 0.2 s to 5 min (see *The Metastable O_H State* in the main text), which would correspond to an activation energy barrier of at least ∼16 kcal/mol at 310 K for the $\mathbf{O_H}\rightarrow\mathbf{O}$ transition. According to the models of $\mathbf{O_H}$ and **O** presented here, this transition would at least include hydrogen-bonding rearrangements, structural rearrangements, and diffusion of a water molecule. The energetic cost of the hydrogen-bonding rearrangement required to form **O** from $\mathbf{O_H}$ was calculated by constructing a variant $\mathbf{O_H}^*$ ($S = 1$) state in which two of the four H bonds were cleaved (Fig. S1). The structure of this state was optimized at the BP86/SVP level of theory, followed by a single-point calculation at the level B3–LYP/TZVP/ε = 4. The energy of this state was found to be ∼10 kcal/mol higher than the $\mathbf{O_H}$ ($S = 1$) state, in accordance with the strength of two strong H bonds (19). The water molecule released by cleaving the two H bonds would then diffuse by 2–3 Å, bind Cu_B, and eventually form state **O**, which is likely to encounter a diffusion-related barrier. Alternatively, if this water molecule is recruited from the "outside," the diffusion-related barrier would be significantly higher owing to the slow diffusion of water molecules in the protein interior (see also *Results* and *Discussion* in the main text). Furthermore, the relaxation of the compact BNC structure in the low-energy $\mathbf{O_H}^3$ state to state **O** would also contribute to the activation barrier. This can be visualized by the energetic differences between the states $\mathbf{O_H}^2{}_{\mathbf{AF}}/\mathbf{O_H}^3$ and $\mathbf{O_H}^2$ (Table S4), where the latter state is structurally closer to the **O** states (e.g., Fe–Cu and Fe–Nε_{His376} distances).

1. Harrenga A, Michel H (1999) The cytochrome *c* oxidase from Paracoccus denitrificans does not change the metal center ligation upon reduction. *J Biol Chem* 274(47): 33296–33299.
2. Tsukihara T, et al. (2003) The low-spin heme of cytochrome *c* oxidase as the driving element of the proton-pumping process. *Proc Natl Acad Sci USA* 100(26):15304–15309.
3. Becke AD (1988) Density-functional exchange-energy approximation with correct asymptotic behavior. *Phys Rev A* 38(6):3098–3100.
4. Perdew JP (1986) Density-functional approximation for the correlation energy of the inhomogeneous electron gas. *Phys Rev B Condens Matter* 33(12):8822–8824.
5. Schäfer A, Horn H, Ahlrichs R (1992) Fully optimized contracted Gaussian basis sets for atoms Li to Kr. *J Chem Phys* 97(4):2571–2577.
6. Schäfer A, Huber C, Ahlrichs R (1994) Fully optimized contracted Gaussian basis sets of triple zeta valence quality for atoms Li to Kr. *J Chem Phys* 100(8):5829–5835.
7. Becke AD (1993) Density-functional thermochemistry. III. The role of exact exchange. *J Chem Phys* 98(7):5648–5652.
8. Lee C, Yang W, Parr RG (1988) Development of the Colle-Salvetti correlation-energy formula into a functional of the electron density. *Phys Rev B Condens Matter* 37(2): 785–789.
9. Stephens PJ, Devlin FJ, Chabalowski CF, Frisch MJ (1994) *Ab initio* calculation of vibrational absorption and circular dichroism spectra using density functional force fields. *J Phys Chem* 98(45):11623–11627.
10. Ahlrichs R, Bär M, Häser M, Horn H, Kölmel C (1989) Electronic-structure calculations on workstation computers—The program system TURBOMOLE. *Chem Phys Lett* 162(3):165–169.
11. Klamt A, Schuurmann G (1993) COSMO: A new approach to dielectric screening in solvents with explicit expressions for the screening energy and its gradient. *J Chem Soc Perkin Trans* 2(5):799–805.
12. Humphrey W, Dalke A, Schulten K (1996) VMD: Visual molecular dynamics. *J Mol Graph* 14(1):33–38, 27–28.
13. Reiss H, Heller A (1985) The absolute potential of the standard hydrogen electrode: A new estimate. *J Phys Chem* 89(20):4207–4213.
14. Mulliken RS (1955) Electronic population analysis on LCAO-MO molecular wave functions. I. *J Chem Phys* 23(10):1833–1840.
15. Noodleman L (1981) Valence bond description of antiferromagnetic coupling in transition metal dimers. *J Chem Phys* 74(10):5737–5743.
16. Soda T, et al. (2000) Ab initio computations of effective exchange integrals for H-H, H-He-H and Mn_2O_2 complex: Comparison of broken-symmetry approaches. *Chem Phys Lett* 319(3-4):223–230.
17. Kitagawa Y, et al. (2007) Approximately spin-projected geometry optimization method and its application to di-chromium systems. *Chem Phys Lett* 442(4-6):445–450.
18. Pantazis DA, Krewald V, Orio M, Neese F (2010) Theoretical magnetochemistry of dinuclear manganese complexes: Broken symmetry density functional theory investigation on the influence of bridging motifs on structure and magnetism. *Dalton Trans* 39(20):4959–4967.
19. Perrin CL, Nielson JB (1997) "Strong" hydrogen bonds in chemistry and biology. *Annu Rev Phys Chem* 48:511–544.

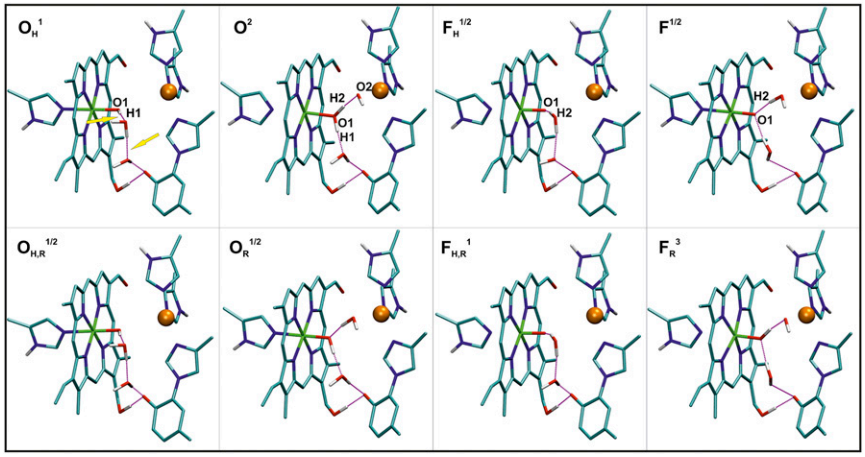

Fig. S1. DFT optimized geometries of different models of the binuclear center. Fe (green), C (cyan), N (blue), O (red), Cu (orange) atoms, and only hydrogen atoms bonded to N and O are shown. H bonds are displayed as purple dotted lines. The upper left corner shows the name of each state, where the superscript denotes the overall spin. Subscript H denotes an activated state without a fourth oxygenous ligand of Cu_B, and subscript R (reduced) indicates that the site has received an additional electron (see opening paragraphs of main text). The two yellow arrows mark the two H bonds that were cleaved by rotating the water molecule hydrogen-bonded to the oxygenous ligand of Fe.

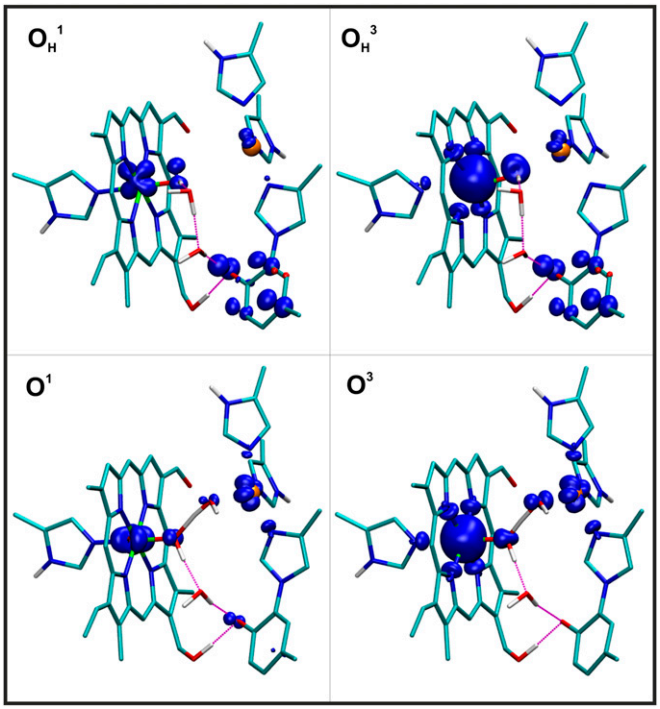

Fig. S2. Spin density distributions in $\mathbf{O_H}$ and **O** states. Excess α density (in blue) and β density (in red) are shown as isocontour plots (0.01 $e/Å^3$). Fe (green), C (cyan), N (blue), O (red), and Cu (orange) atoms are shown in licorice representation. Only hydrogen atoms bonded to N and O are shown. H bonds are displayed as purple dotted lines.

Table S1. Model systems and their total charge (q) and total spin (S)

Model	q*	$S^{\dagger}$	Model	Q	S
$\mathbf{O_H}$			**O**		
$\mathbf{O_H^{0}}$ ‡,§	1	0	$\mathbf{O^0}$	1	0
$\mathbf{O_H^{1}}$	1	1	$\mathbf{O^1}$	1	1
$\mathbf{O_H^{2}}$	1	2	$\mathbf{O^2}$	1	2
$\mathbf{O_H^{3}}$	1	3	$\mathbf{O^3}$	1	3
$\mathbf{F_H}$			**F**		
$\mathbf{F_H^{1/2}}$	1	1/2	$\mathbf{F^{1/2}}$	1	1/2
$\mathbf{F_H^{3/2}}$	1	3/2	$\mathbf{F^{3/2}}$	1	3/2
$\mathbf{F_H^{5/2}}$	1	5/2	$\mathbf{F^{5/2}}$	1	5/2
$\mathbf{O_{H,R}}$			$\mathbf{O_R}$		
$\mathbf{O_{H,R}^{1/2}}$	0	1/2	$\mathbf{O_R^{1/2}}$	0	1/2
$\mathbf{O_{H,R}^{3/2}}$	0	3/2	$\mathbf{O_R^{3/2}}$	0	3/2
$\mathbf{O_{H,R}^{5/2}}$	0	5/2	$\mathbf{O_R^{5/2}}$	0	5/2
$\mathbf{F_{H,R}}$			$\mathbf{F_R}$		
$\mathbf{F_{H,R}^{0}}$	0	0	$\mathbf{F_R^{0}}$	0	0
$\mathbf{F_{H,R}^{1}}$	0	1	$\mathbf{F_R^{1}}$	0	1
$\mathbf{F_{H,R}^{2}}$	0	2	$\mathbf{F_R^{2}}$	0	2
$\mathbf{F_{H,R}^{3}}$	0	3	$\mathbf{F_R^{3}}$	0	3

*The total charge of system is calculated by adding charges on individual systems; Fe[IV] (+4) or Fe[III] (+3), porphyrin (–2), Cu_B (+2 for oxidized or +1 for reduced), hydroxyl (–1), oxygenous ligand in ferryl state (–2), and tyrosinate (–1).

†The total spin of the system is calculated from individual spins of metal systems in different redox states; Fe[III] (S = 1/2, 3/2, or 5/2), Fe[IV] (S = 0, 1, or 2), and Cu[II] (S = 1/2).

‡The total spin of the model is indicated in the superscript.

§The H subscript in the $\mathbf{O_H}$ state denotes the hydroxyl ligand of heme a_3 Fe (see *The Metastable O_H State* in the main text). For all other states, subscript H is retained for consistency and to distinguish them from inactivated four-coordinated states (**O**, **F**, $\mathbf{O_R}$, and $\mathbf{F_R}$).

Table S2. Geometric data (distances in ångströms and angles in degrees)

Models	Fe–N$\varepsilon_{His376*}$	Fe–Cu	Fe–O1[†]	Cu–O2[†]	Dihedral[‡]
O_H^1	2.07	5.17	1.78		9.4
O_H^2	2.14	5.14	1.77		9.5
O_H^3	2.57	4.01	1.96	(2.17)[§]	29.0
O^1	2.02	5.42	1.82	2.11	20.0
$O^{2¶}$	2.27	5.21	2.07	1.97	22.0
$O^{3¶}$	2.26	5.18	1.99	1.99	21.7
$F_H^{1/2}$	2.14	5.05	1.66		10.6
$F_H^{3/2}$	2.14	5.05	1.66		10.6
$F_H^{5/2}$	2.15	5.04	1.66		10.4
$F^{1/2}$	2.08	5.35	1.67	2.18	18.3
$F^{3/2}$	2.08	5.35	1.67	2.18	18.3
$F^{5/2}$	2.09	5.32	1.67	2.16	18.6
$O_{H,R}^{1/2}$	2.08	4.93	1.81		10.8
$O_{H,R}^{3/2}$	2.09	5.01	1.76		9.7
$O_{H,R}^{5/2}$	2.61	3.90	1.94		31.5
$O_R^{1/2}$	2.02	5.38	1.83	2.17	20.4
$O_R^{3/2}$	2.03	5.35	1.80	2.13	20.0
$O_R^{5/2}$	2.33	5.17	1.90	2.13	21.0
$F_{H,R}^1$	2.13	5.09	1.65		9.8
$F_{H,R}^2$	2.16	5.04	1.65		10.3
$F_{H,R}^3$	2.17	5.00	1.66		10.9
F_R^1	2.09	5.30	1.68	2.21	18.2
F_R^2	2.10	5.25	1.67	2.14	19.8
F_R^3	2.43	4.94	1.84	1.96	22.7

*Proximal histidine ligand of heme iron.

[†]O1 and O2 are the oxygen atoms ligating Fe and Cu, respectively, as shown in Fig. S1.

[‡]Dihedral angle is Nδ_{His244}–Nε_{His291}–Nε_{His290}–Cu_B.

[§]Cu_B–O1 distance in μ-hydroxo–bridged Fe[III]/Cu[II].

[¶]Structure optimized to Fe[III]–OH_2...HO–Cu[II] (Fig. S1).

Table S3. Spin densities

Models	Fe	O1*	Cu	O2†	Tyr‡
$O_{H\ OSS/AF}^{0}$ §	−1.04	−0.04	0.16	—	0.76
O_{H}^{1}	0.93	0.16	0.12	—	0.74
$O_{H\ AF}^{1}$	2.86	0.21	−0.28	—	−0.58
O_{H}^{2}	2.75	0.16	0.10	—	0.76
$O_{H\ AF}^{2}$	4.27	0.24	−0.24	—	−0.63
O_{H}^{3}	4.26	0.25	0.20	—	0.74
$O_{OSS/AF}^{0}$	−1.11	0.0	0.63	0.13	0.0
O^{1}	1.00	0.08	0.55	0.04	0.20
O_{AF}^{1}	2.94	0.10	−0.63	−0.13	0.0
O^{2}	2.91	0.08	0.62	0.16	0.0
O_{AF}^{2}	4.32	0.11	−0.64	−0.12	0.0
O^{3}	4.32	0.12	0.63	0.14	0.0
$F_{H}^{1/2}$	1.35	0.73	−0.07	—	−0.86
$F_{H\ AF}^{1/2}$	1.37	0.73	−0.05	—	−0.87
$F_{H}^{3/2}$	1.35	0.73	0.07	—	0.85
$F_{H\ AF}^{3/2}$	3.26	0.50	−0.05	—	−0.88
$F_{H}^{5/2}$	3.26	0.50	0.06	—	0.87
$F^{1/2}$	1.53	0.57	−0.31	0.0	−0.55
$F_{AF}^{1/2}$	1.56	0.57	−0.28	0.0	−0.57
$F^{3/2}$	1.53	0.57	0.31	0.02	0.55
$F_{AF}^{3/2}$	3.35	0.40	−0.28	−0.01	−0.58
$F^{5/2}$	3.34	0.40	0.30	0.01	0.55
$O_{H,R}^{1/2}$	0.93	0.15	0.0	—	0.0
$O_{H,R}^{3/2}$	2.72	0.14	0.0	—	0.0
$O_{H,R}^{5/2}$	4.23	0.27	0.07	—	0.0
$O_{R}^{1/2}$	0.98	0.09	0.0	0.0	0.0
$O_{R}^{3/2}$	2.71	0.25	0.0	0.0	0.0
$O_{R}^{5/2}$	4.28	0.25	0.0	0.01	0.0
$F_{H,R\ OSS/AF}^{0}$	−1.37	−0.71	0.02	—	0.41
$F_{H,R}^{1}$	1.30	0.78	0.0	—	0.0
$F_{H,R\ AF}^{1}$	1.34	0.75	0.0	—	0.0
$F_{H,R}^{2}$	3.23	0.52	0.0	—	0.0
$F_{H,R\ AF}^{2}$	3.26	0.50	0.0	—	0.0
$F_{H,R}^{3}$	3.43	0.51	0.02	—	0.37
$F_{R\ OSS/AF}^{0}$	−1.01	−0.06	0.60	0.18	0.0
F_{R}^{1}	1.48	0.61	0.0	0.01	0.0
$F_{R\ AF}^{1}$	2.74	0.30	−0.61	−0.18	0.0
F_{R}^{2}	3.28	0.40	0.04	0.01	0.0
$F_{R\ AF}^{2}$	4.24	0.33	−0.61	−0.17	0.0
F_{R}^{3}	4.23	0.34	0.60	0.19	0.0

*The oxygen atom ligating the iron.
†The oxygen atom ligating the Cu_B.
‡Cross-linked tyrosine.
§OSS/AF, open-shell singlet/antiferromagnetic.

Table S4. Energies (E in kcal/mol) of various model systems

Models	E	Models	E
$O^0_{HOSS/AF}$ *	38.5	$O^0_{OSS/AF}$	10.1
O^1_H	16.1	O^1	0.2
$O^1_{H\ AF}$	25.5	O^1_{AF}	7.6
O^2_H	28.2	O^2	0
$O^2_{H\ AF}$	16.9	O^2_{AF}	3.9
O^3_H	19.4	O^3	3.8
$F^{1/2}_H$	5.0	$F^{1/2}$	0
$F^{1/2}_{H\ AF}$	8.8	$F^{1/2}_{AF}$	4.41
$F^{3/2}_H$	5.0	$F^{3/2}$	0
$F^{3/2}_{H\ AF}$	17.9	$F^{3/2}_{AF}$	14.74
$F^{5/2}_H$	17.8	$F^{5/2}$	14.71
$O^{1/2}_{H,R}$	6.9	$O_R{}^{1/2}$	0
$O^{3/2}_{H,R}$	29.2	$O_R{}^{3/2}$	25.1
$O^{5/2}_{H,R}$	13.8	$O_R{}^{5/2}$	9.2
$F^0_{H,R\ OSS/AF}$	40.4	$F^0_{R\ OSS/AF}$	14.3
$F^1_{H,R}$	2.5	F^1_R	1.7
$F^1_{H,R\ AF}$	11.6	$F^1_{R\ AF}$	11.2
$F^2_{H,R}$	14.6	F^2_R	24.3
$F^2_{H,R\ AF}$	17.3	$F^2_{R\ AF}$	−0.03
$F^3_{H,R}$	47.8	F^3_R	0

The energies (E) reported in the table are obtained at the B3LYP/def2–TZVP/$\varepsilon = 4$ level of theory. The energies of all O_H and O, F_H and F, $O_{H,R}$ and O_R, and $F_{H,R}$ and F_R states are relative to O^2, $F^{1/2}$, $O_R^{1/2}$, and F_R^3, respectively.
*OSS/AF, open-shell singlet/antiferromagnetic.